

Article

Seismic Response of a Three-Dimensional Asymmetric Multi-Storey Reinforced Concrete Structure

Hyun-Kyu Lim ¹, Jun Won Kang ^{1,*}, Hongrak Pak ¹ , Ho-Seok Chi ², Young-Geun Lee ² and Janghwan Kim ³

¹ Department of Civil Engineering, Hongik University, Seoul 04066, Korea; HKL@daelim.co.kr (H.-K.L.); juniorceo@naver.com (H.P.)

² Department of Structural Systems & Site Safety Evaluation, Korea Institute of Nuclear Safety, Daejeon 34142, Korea; hsc@kins.re.kr (H.-S.C.); k730lyg@kins.re.kr (Y.-G.L.)

³ Daelim Industrial Corporation Ltd., Seoul 03152, Korea; janghwan.kim1@gmail.com

* Correspondence: jwkang@hongik.ac.kr; Tel.: +82-2-320-1601

Received: 28 January 2018; Accepted: 19 March 2018; Published: 22 March 2018



Featured Application: Authors are encouraged to provide a concise description of the specific application or a potential application of the work. This section is not mandatory.

Abstract: This study discusses the seismic behavior of a geometrically asymmetric three-storey reinforced concrete (RC) building, considering torsional effect and material nonlinearity. The building is a test structure that was used for seismic performance evaluation in the SMART 2013 (Seismic design and best-estimate Methods Assessment for Reinforced concrete buildings subjected to Torsion and nonlinear effects) international benchmark. To begin with, nonlinear stress–strain relationships that were set up for concrete and reinforcing steel are validated by finite element local tests with a representative volume element. A modal analysis shows that the first three calculated natural frequencies are close to the ones that are obtained by modal experiments. The finite element modeling is further validated by comparing the calculated displacement and acceleration due to a low-intensity ground motion with the responses from the corresponding shaking table test. Using the validated model, a blind nonlinear seismic analysis is performed for a series of Northridge earthquakes in order to estimate the behavior of the asymmetric RC structure to high-intensity ground motions. The calculated displacement and acceleration, as well as their response spectra at various sampling points, agree well with the results of a three-dimensional benchmark shaking table test. By investigating the seismic torsional behavior of the asymmetric RC structure, it is shown that the seismic response of an asymmetric structure is larger than that of a hypothetical symmetric structure. The result indicates that a larger seismic response should be considered in the seismic design of an asymmetric structure compared to a symmetric structure with similar design conditions.

Keywords: asymmetric reinforced concrete structure; SMART 2013 international benchmark; finite element model; nonlinear seismic analysis; seismic torsional behavior

1. Introduction

The evaluation of the inelastic response of reinforced concrete (RC) structures is essential for estimating the strength and damage of the structure under extreme loads such as earthquake, impact, and blast. In recent years, predicting the large deformation of RC structures has become more practicable, due to the advance of state-of-the-art numerical algorithms and computational power [1–9]. In recent decades, the feasibility of numerical methods for predicting the nonlinear behavior of RC

structures have been assessed through many benchmark campaigns conducted on RC shear walls, columns, and buildings. In 1997, the Nuclear Power Engineering Corporation of Japan organized a series of shaking table tests on regular and U-shaped low-span RC shear walls [10,11]. The results demonstrated the necessity of improving the nonlinear analysis methods for shear walls when dealing with beyond design basis earthquake. From 1997 to 1998, the Commissariat à l'énergie atomique et aux énergies alternatives (CEA) of France performed SAFE (Structure Armées Faiblement Elancées) tests for the experimental characterization of the dynamic behavior of low-span shear walls [12,13]. The SAFE tests were pseudodynamic tests where shear cracking, failure modes, nonlinear load versus displacement diagrams, and wall ductility were confirmed under various earthquake loadings beyond the design level. Other experimental campaigns were conducted by the CEA, such as Conception et Analyse Sismique des Structures en Béton Armé (CASSBA) tests from 1990 to 1993 [14] and CAMUS tests from 1996 to 2002 [15]. These tests were shaking table tests that were conducted on multi-storey mock-ups with lightly reinforced concrete walls. These campaigns helped improve knowledge on the seismic behavior of RC structural systems and provided reference data for model development and validation [16,17]. In 2006, the Network for Earthquake Engineering Simulation (NEES) launched a blind prediction contest on the seismic response of a seven-storey full-scale RC building with cantilever structural walls [18]. The contest program examined the seismic behavior of RC structural systems with particular emphasis on the interaction among walls, slabs, and other gravity systems [19–22].

To improve on the previous development of benchmark campaigns for RC structures, a new benchmark project named SMART 2013 (Seismic design and best-estimate Methods Assessment for Reinforced concrete buildings subjected to Torsion and nonlinear effects) was carried out by the CEA from 2011 to 2015. This project consisted of shaking table tests and an international benchmark analysis on a reduced-scale model ($\frac{1}{4}$ scale) that was representative of a typical half part of a nuclear facility building. The objective of the experimental campaign and benchmark analysis was to evaluate the conventional design method of RC structures for seismic loadings and compare the structural dynamic responses, as well as the floor response spectra, from various benchmark participants. The SMART 2013 campaign used a real high-intensity seismic load that was composed of a series of Northridge earthquakes followed by aftershocks. The benchmark participants used the load data at eight actuator locations of a three-dimensional shaking table to calculate the numerical response of the RC structure and compare it with the experimental result. Before SMART 2013, there was a SMART 2008 benchmark organized by the CEA with similar projects. However, SMART 2013 has the following new features compared to SMART 2008: (i) input signals are real ones and not synthetic ones; (ii) aftershock seismic loading is considered; and (iii) additional load data at the actuator location are provided to benchmark participants.

This study aims to investigate the seismic behavior of the asymmetric SMART 2013 RC building structure, considering torsional effect and material nonlinearity. In particular, the study includes benchmark simulations comprising modal, linear, and nonlinear seismic analyses of the RC structure. First, using mechanical parameters provided by the SMART 2013 international benchmark [23–26], nonlinear constitutive models of concrete and reinforcing steel are constructed. The material models are validated by local tests on a representative volume element (RVE). Then, a finite element (FE) modeling of the entire SMART 2013 RC structure, which is based on its detailed drawings, is validated by comparing the modal and linear time history analysis results with the experimental results. The validated finite element model is used for a blind nonlinear seismic benchmark analysis of the RC structure subjected to the high-intensity Northridge earthquake. Displacement and acceleration, as well as their frequency spectra, are presented, exhibiting the torsional and flexural behaviors of the structure. The computed seismic responses are compared with the results of a shaking table test, which was conducted as part of the benchmark. Finally, the effect of the torsional behavior of the asymmetric RC structure is examined by comparing the seismic response of the asymmetric structure with that of a hypothetical symmetric structure with similar design conditions.

2. Configuration of the Asymmetric RC Building Structure

The SMART 2013 structure is an asymmetric three-storey RC building that is representative of a typical half part of a nuclear facility building at $\frac{1}{4}$ scale, as shown in Figure 1. Due to the asymmetric shape, the structure may exhibit coupled flexural and torsional behaviors against external loads. Figure 2 shows the plan and elevation views of the structure. The principal dimensions of the structural components are presented in Table 1.



Figure 1. The asymmetric three-storey reinforced concrete building used for the SMART (Seismic design and best-estimate Methods Assessment for Reinforced concrete buildings subjected to Torsion and nonlinear effects) 2013 international benchmark campaign.

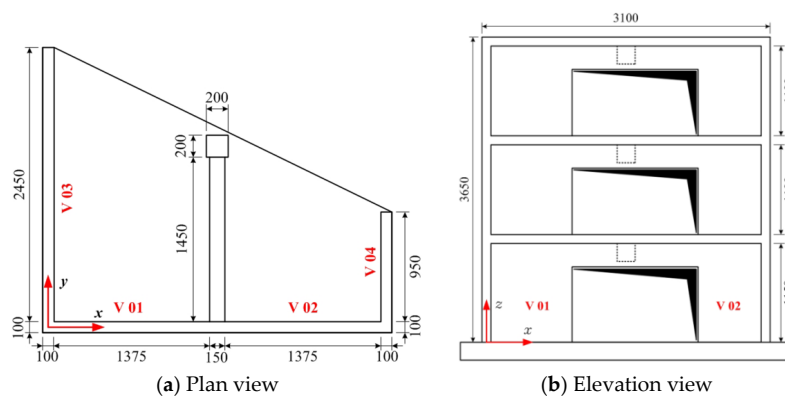


Figure 2. Plan and elevation views of the SMART 2013 reinforced concrete (RC) structure (unit: mm).

Table 1. Dimensions of the structural components of the SMART (Seismic design and best-estimate Methods Assessment for Reinforced concrete buildings subjected to Torsion and nonlinear effects) 2013 reinforced concrete (RC) structure.

Structural Component	Length (mm)	Thickness (mm)	Height (mm)
Wall (V01 + V02)	3100	100	3650
Wall V03	2550	100	3650
Wall V04	1050	100	3650
Beams	1450	150	325
Column	200	200	3900

The SMART 2013 RC structure was designed according to the French nuclear regulations and guidelines. The design is based on a design acceleration spectrum for 5% structural damping. The design spectrum is based on a ground motion with the peak ground acceleration (PGA) of 0.2 g, which corresponds to an earthquake with a Richter magnitude of 5.5 and an epicenter distance of 10 km [23]. The foundation of the wall is made of a continuous RC footing with a width of 65 cm and a

height of 25 cm, as shown in Figure 3a. There are 34 anchoring points through which threaded steel rods with a 36 mm diameter connect the foundation to the shaking table. Figure 3b shows a cutaway view of the foundation. The center column of the structure is anchored to the shaking table with a connecting steel plate that is 2 mm thick.

The mass of the SMART 2013 RC building is about 11.89 t. To reflect the weight of the equipment and pipelines, additional mass is considered for each floor. Mass scaling is considered when applying the additional mass to floors, since the building is a quarter-scale structure [23]. The additional mass is 11.45 t for the first floor, 12.17 t for the second floor, and 10.32 t for the third floor. The total mass of the structure with the additional floor mass is about 45 t. The shaking table is connected to eight hydraulic actuators, out of which four are placed in a horizontal direction and the remaining four are laid in a vertical direction. The SMART 2013 structure is placed on the shaking table such that its center of mass corresponds approximately to that of the shaking table. Figure 4 shows the SMART 2013 structure positioned on the shaking table, as well as the eight actuator locations. The ground motion is applied to the actuator locations at the side and bottom of the shaking table using a displacement control method. Figure 5 shows the sampling points on each floor where displacement and acceleration are recorded.

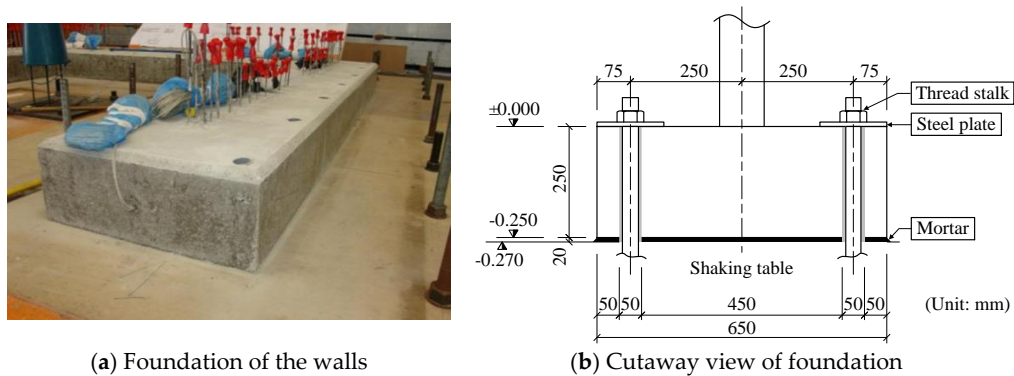


Figure 3. Wall foundation of the SMART 2013 RC structure [23]; (a) RC footing; (b) cutaway view.

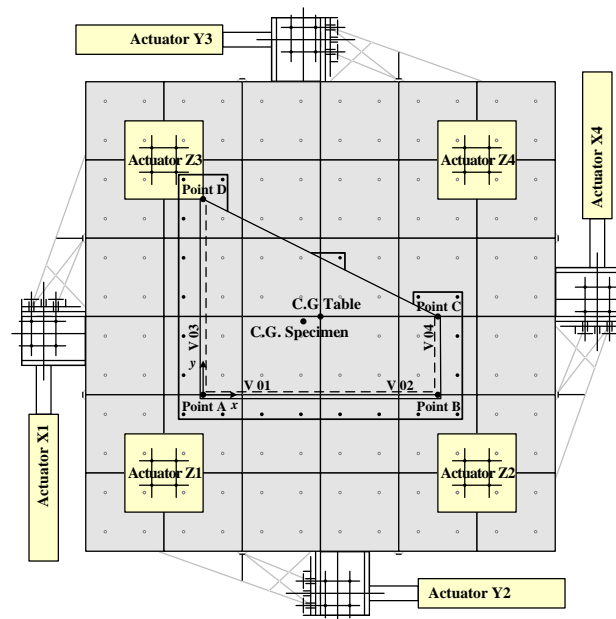


Figure 4. Plan view of the SMART 2013 structure positioned on the shaking table [23]; four hydraulic actuators (X1, X4, Y2, Y3) are placed in a horizontal direction, and the other four (Z1, Z2, Z3, Z4) are laid in a vertical direction.

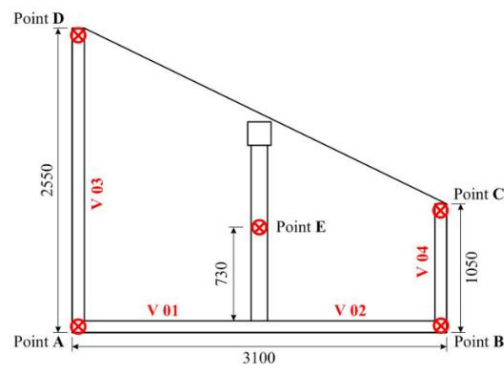


Figure 5. Response sampling points on each floor (unit: mm).

3. Finite Element Modeling of the SMART 2013 RC Structure

3.1. Constitutive Models for Concrete and Steel Reinforcement

To capture the inelastic stress–strain behavior of the RC members, nonlinear constitutive models of concrete and rebar are needed. Equations (1) and (2) represent a widely used uniaxial compressive stress–strain relationship for concrete [27]:

$$\sigma = \frac{E_c \epsilon}{1 + \left(\frac{\epsilon}{\epsilon_0}\right)^2} \tag{1}$$

$$\epsilon_0 = \frac{2f'_c}{E_c} \tag{2}$$

where σ and ϵ denote stress and strain, respectively, E_c denotes the initial Young’s modulus of concrete, and f'_c is the ultimate compressive strength of concrete. ϵ_0 represents the strain at the compressive strength f'_c . Table 2 lists the measured material properties of concrete and rebar. Based on Equation (1), a simplified multilinear stress–strain curve of concrete is constructed using the material properties of Table 2. For steel reinforcement, an elastic–perfectly plastic stress–strain curve is also constructed by referring to the property values in Table 2. Figure 6 shows the simplified strain–stress curves for each of the constitutive models. These curves are incorporated into ANSYS Mechanical APDL [28], a finite element analysis package, as the multilinear constitutive relationship of concrete with isotropic hardening and the elastoplastic constitutive relationship of steel reinforcement, respectively. The concrete model consists of six linear segments with an initial Young’s modulus of 32,000 MPa and successively decreasing moduli. The compressive and tensile strengths of concrete are 30 MPa and 2.4 MPa, respectively. The stress–strain curve starts from zero stress and strain. It is assumed that concrete behaves in a linearly elastic manner up to Point 1, at which the stress is $0.3f'_c$. Points 2, 3, and 4 are obtained from Equation (1), where ϵ_0 is calculated by Equation (2). Point 5 is at f'_c and ϵ_0 . The stress–strain curve is extended to Point 6, where the strain is 0.003, with a slight increase of stress to help the convergence of solutions in the nonlinear seismic analysis with ANSYS. The yield strength of the rebar is 500 MPa at the strain of 0.00238 in both tension and compression.

Table 2. Material properties of concrete and rebar obtained by experiments [24].

Structural Component	Young’s Modulus (MPa)	Poisson’s Ratio	Compressive Strength (MPa)	Tensile Strength (MPa)	Mass Density (kg·m ⁻³)
Foundation concrete	25,400	0.17	43.3	3.45	2300
Slab concrete on the first floor	28,200	0.18	41.1	3.25	2300
Slab concrete on the second floor	24,700	0.17	36.8	3.35	2300
Slab concrete on the third floor	24,400	0.18	37.8	3.40	2300
Wall concrete	28,700	0.19	41.7	3.89	2300
Steel reinforcement	267,333	0.30	528	528	7800

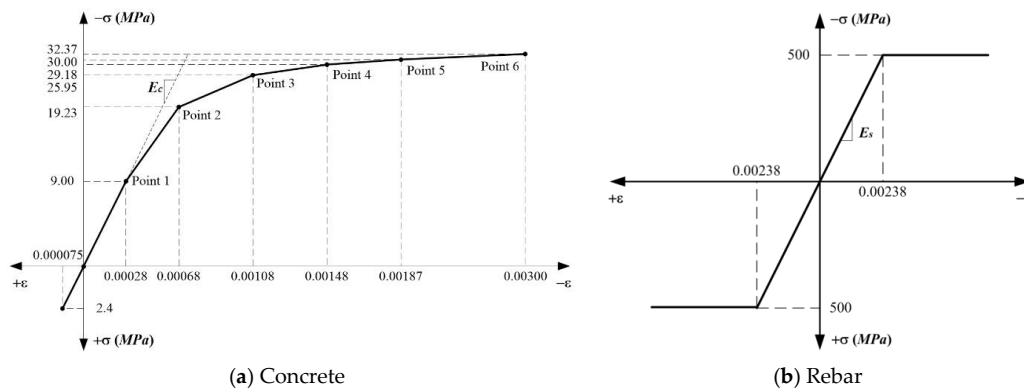


Figure 6. Strain–stress curves for concrete and steel reinforcement.

3.2. Failure Criterion for Concrete

For the simulation of the behavior of concrete materials in multiaxial stress states, the Willam–Warnke failure criterion [29] was implemented in ANSYS with a SOLID65 element (ANSYS Mechanical APDL Release 14.5, ANSYS Inc., Canonsburg, PA, USA, 2012), which is a three-dimensional hexahedral element that can be used to model concrete. Both cracking and crushing failure modes can be accounted for by using the failure criterion. In the concrete element, cracking occurs when the principal tensile stress lies outside the failure surface. On the other hand, crushing occurs when all of the principal stresses are compressive and lie outside the failure surface. The Willam–Warnke failure criterion prescribes the portion of the failure curve in deviatoric plane as part of an elliptic curve. The cylindrical von Mises model and the conical Drucker–Prager model are all special cases of the Willam–Warnke failure criterion. The three-parameter Willam–Warnke failure surface can be expressed as:

$$f(\sigma_m, \tau_m, \theta) = \frac{1}{\rho} \frac{\sigma_m}{f'_c} + \frac{1}{r(\theta)} \frac{\tau_m}{f'_c} - 1 = 0 \tag{3}$$

where f'_c is the uniaxial compressive strength of concrete, while σ_m and τ_m denote the mean normal and mean shear stresses, respectively. The variable θ denotes the angle of similarity. They can be represented as:

$$\sigma_m = \frac{1}{3} I_1, \tau_m = \sqrt{\frac{2}{5}} \sqrt{J_2}, \theta = \frac{1}{3} \cos^{-1} \left(\frac{3\sqrt{3}J_3}{2J_2^{\frac{3}{2}}} \right) \tag{4}$$

where I_1 is the first invariant of the stress tensor, while J_2 and J_3 are the second and third invariants of the deviatoric part of the stress tensor, respectively. In Equation (3), $r(\theta)$ is the radial coordinate of the failure surface on the deviatoric plane, which can be expressed as the following:

$$r(\theta) = \frac{2r_c(r_c^2 - r_t^2) \cos \theta + r_c(2r_t - r_c) [4(r_c^2 - r_t^2) \cos^2 \theta + 5r_t^2 - 4r_t r_c]^{\frac{1}{2}}}{4(r_c^2 - r_t^2) \cos^2 \theta + (r_c - 2r_t)^2} \tag{5}$$

The parameters ρ , r_c , and r_t in Equations (3) and (5) are the three parameters of the Willam–Warnke failure surface model. The parameters r_c and r_t are the magnitude of the position vectors at locations $\theta = 0$ and $\pi/3$ on the deviatoric plane, respectively, as shown in Figure 7. The three model parameters can be expressed as:

$$\rho = \frac{\bar{f}'_{bc} \bar{f}'_t}{\bar{f}'_{bc} - \bar{f}'_t} \tag{6}$$

$$r_c = \sqrt{\frac{6}{5}} \frac{\bar{f}'_{bc} \bar{f}'_t}{3\bar{f}'_{bc} \bar{f}'_t + \bar{f}'_{bc} - \bar{f}'_t} \tag{7}$$

$$r_t = \sqrt{\frac{6}{5}} \frac{\bar{f}'_{bc} \bar{f}_t}{2\bar{f}'_{bc} + \bar{f}_t} \tag{8}$$

In Equations (6)–(8), \bar{f}_t and \bar{f}'_{bc} are the strength ratios, which are represented as:

$$\bar{f}_t = \frac{f_t}{f'_c}, \bar{f}'_{bc} = \frac{f'_{bc}}{f'_c} \tag{9}$$

where f_t and f'_{bc} are the uniaxial tensile strength and the equal biaxial compressive strength of concrete, respectively. Figure 8 shows the trace of the three-parameter Willam–Warnke yield surface in the σ_1 - σ_2 principal coordinate plane for $\bar{f}_t = 0.1$ and $\bar{f}'_{bc} = 1.16$.

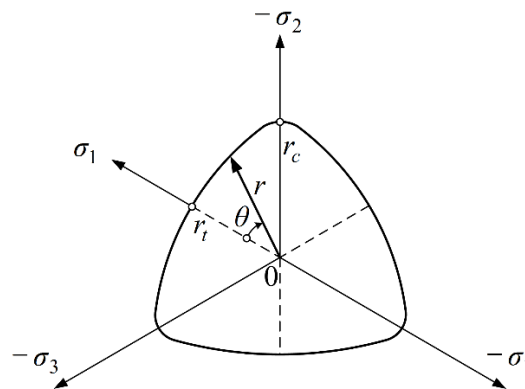


Figure 7. Deviatoric section of the Willam–Warnke failure surface.

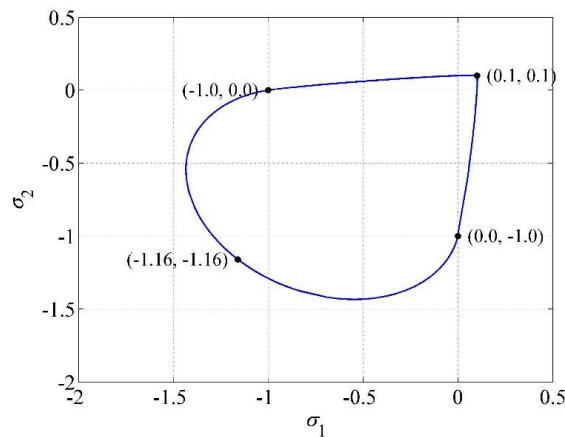


Figure 8. Trace of the three-parameter Willam–Warnke yield surface in the σ_1 - σ_2 plane for $\bar{f}_t = 0.1$ and $\bar{f}'_{bc} = 1.16$.

3.3. Finite Element Modeling of Concrete and Steel Reinforcement

For the finite element modeling of concrete, the SOLID65 three-dimensional element of ANSYS was used, which is associated with the plasticity algorithm described in Section 3.2. The solid element had eight nodes, with three translational degrees of freedom at each node. Several material property data are required for SOLID65: elastic modulus E , uniaxial compressive strength f'_c , uniaxial tensile strength f_t , Poisson’s ratio ν , shear transfer coefficient β , and the uniaxial constitutive relationship as described in Section 3.1. The shear transfer coefficient β ranged from 0 to 1, with 0 representing the complete loss of shear transfer along the crack face, and 1 representing no loss of shear transfer. The shear transfer coefficient used in this study was 0.5 for an open crack and 0.9 for a closed crack.

For the finite element modeling of steel reinforcement, a three-dimensional beam element, BEAM188, of ANSYS was used, for which the elastic–perfectly plastic constitutive relationship described in Section 3.1 was imposed. The reinforcing steel element was set to share the node with a concrete element in order to model a perfect bond between concrete and reinforcing steel.

3.4. Local Test

To validate the feasibility of the constitutive models, a local finite element test was performed on the RVEs. The local test consisted of uniaxial and biaxial cyclic loading tests on a concrete RVE, and a shear test on an RC RVE. The concrete RVE was a cube with a side length of 1 m, and the RC RVE was a cuboid with side lengths of 200 mm and a width of 10 mm, as shown in Figure 9. The local test configuration is described in Table 3. Figures 10 and 11 show the boundary condition of the RVEs and the time history of cyclic loads, respectively, for local tests rc.1 and rc.2.

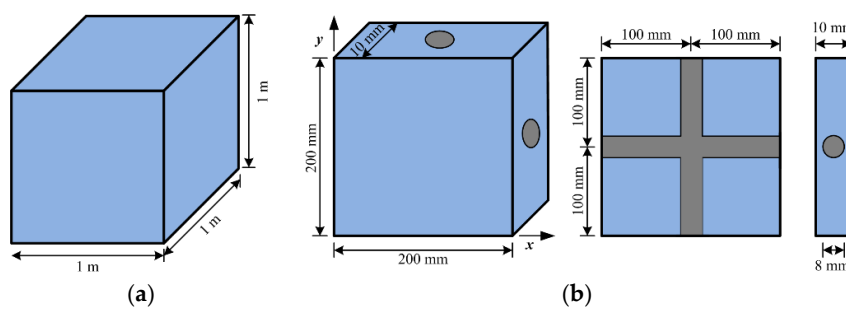


Figure 9. Representative volume elements for local finite element test; (a) Concrete representative volume element (RVE); (b) RC RVE.

Table 3. Configuration of the local test. RVE: representative volume element.

Test No.	Material	Aim	Loading Conditions
c.1	Concrete	Construct failure surface	Biaxial tension–compression loading from –35 MPa to 2.4 MPa
rc.1	Reinforced concrete	Identify axial cyclic response of RC RVE	Uniaxial cyclic tension–compression loading with displacement ranging from –4 mm to 1.5 mm
rc.2	Reinforced concrete	Identify shear cyclic response of RC RVE	Cyclic pure shear loading with the force ranging from –6 kN to 6 kN

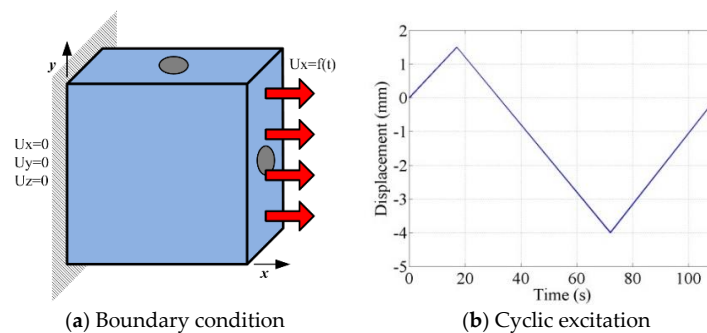


Figure 10. Local test rc.1: uniaxial cyclic displacement loading.

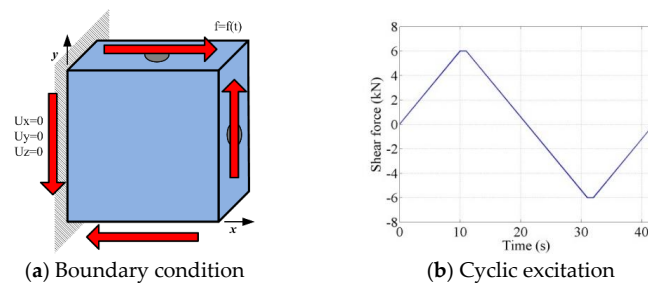


Figure 11. Local test rc.2: cyclic pure shear loading.

Figure 12 shows the yield and failure surfaces constructed from local test c.1 on the concrete RVE. The failure surface was constructed with the biaxial normal stresses where compressive crushing or tensile cracking occurred. In the case of equal biaxial loading, principal stresses in both x_1 and x_2 directions reached about $1.16f'_c$ at compressive failure, which shows the feasibility of the nonlinear material modeling in Sections 3.1 and 3.2. Figure 13 shows the stress–strain response from local tests rc.1 and rc.2 on the RC RVE. The stress–strain response from the local test rc.1 was nonlinear because of the large deformation of the RVE, whereas the shear response from the test rc.2 remained linear. The local test showed that the material models of concrete and rebar worked well in the finite element analysis.

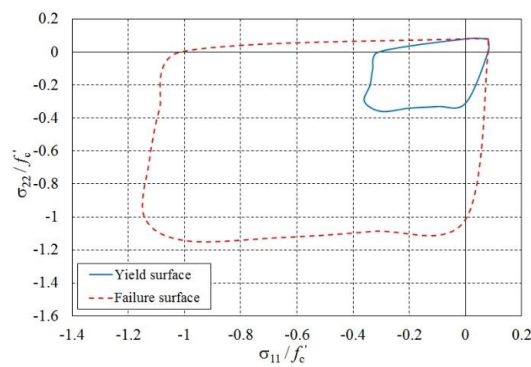


Figure 12. Yield and failure surfaces constructed from local test c.1.

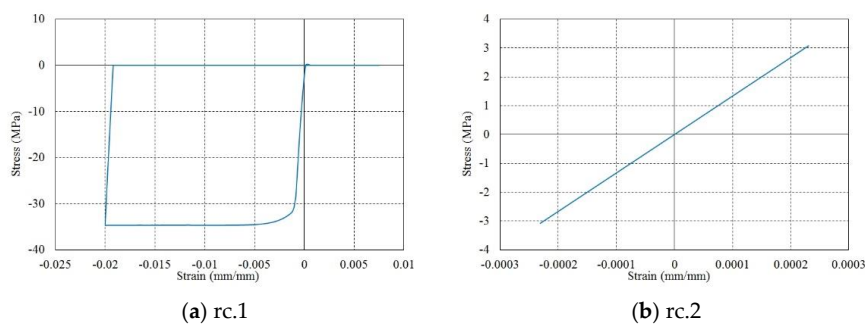


Figure 13. Stress–strain responses from local tests rc.1 and rc.2.

3.5. Finite Element Models of Structural Components

The SMART 2013 RC building consists of eight structural components: foundation, wall, slab, beam, column, rebar, steel plate, and shaking table. The rebar and steel plate are modeled with BEAM188 and SOLID185 elements, respectively, and the remaining six components are modeled with SOLID65 concrete element. SOLID185 is an eight-node solid element in ANSYS that is capable of modeling large deformation and stress stiffening. The rebar element was set to share the node with a

concrete element in order to model the perfect bond between the two elements. Table 4 summarizes the total number of elements, the total number of nodes, and the number of solid and beam elements. Figure 14a shows the full structural model of the mock-up structure, including the shaking table. Figure 14b shows the rebar elements in the concrete slabs, walls, beams, and the column. Figure 14c–f exhibits modeling details for the slab connected to the column, the slab supported by floor beams, and the reinforcement in walls and slabs, respectively.

Table 4. Geometrical characteristics of the finite element (FE) model.

Geometrical Characteristics of the FE Model	Number
Total number of elements	13,391
Total number of nodes	14,479
Number of solid elements	11,007
Number of beam elements	2384

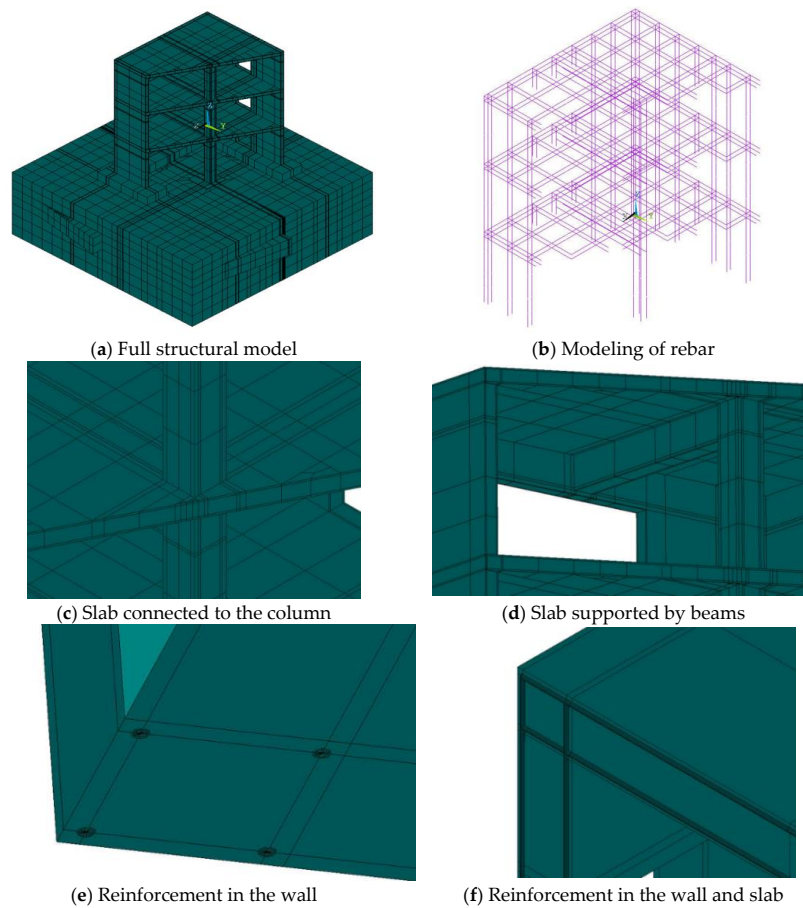


Figure 14. Finite element modeling of the SMART 2013 RC structure.

4. Validation of the Finite Element Model

4.1. Modal Analysis

In order to validate the finite element modeling of the SMART 2013 RC structure, natural frequencies calculated by modal analysis were compared with those obtained by experiment. In the modal analysis, three different model configurations were investigated. In Case 1, the mock-up structure was fixed at the foundation level with no additional mass. In Case 2, the structure was fixed at the foundation level, and loaded with the additional mass on each floor. In Case 3, the structure was

connected to the shaking table and loaded with the additional mass on each floor, similar to Case 2. The actuator locations were set as fixed boundaries. Table 5 presents the first three natural frequencies that were calculated for each model case, along with the experimentally obtained natural frequencies for Case 3 [30–33]. The computed first three natural frequencies for the Case 3 were 6.26 Hz, 7.77 Hz, and 13.15 Hz, respectively, and they are close to the experiment results. The modal analysis used a reduced integration method in order to reduce the stiffness of the RC structure, and thus relieve the stiffer simulation that results when solid elements are used. The reduced integration method was also used in the subsequent seismic simulation. Figures 15–17 show the mode shape for each case of model configurations. The first and second modes were bending modes to x - and y -axes, respectively, while the third mode is a torsional mode to the z -axis. As seen in the figures, the structure exhibited torsional behavior in all three modes because of its asymmetrical shape.

Table 5. Natural frequencies of the SMART 2013 RC structure for three model cases.

	Model Configurations	First Modal Frequency (Hz)	Second Modal Frequency (Hz)	Third Modal Frequency (Hz)
Analysis	Case 1	21.37	36.23	65.82
	Case 2	8.93	15.39	30.71
	Case 3	6.26	7.77	13.15
Experiment	Case 3	6.28	7.86	16.50

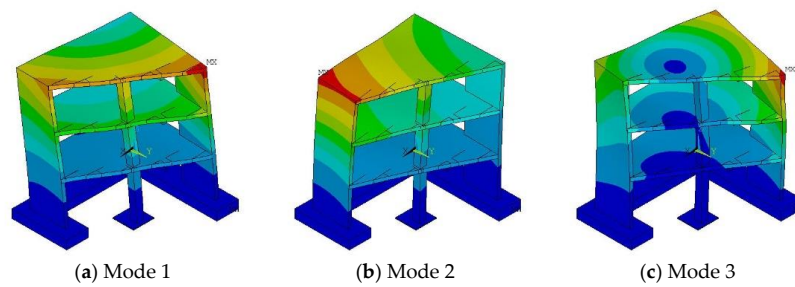


Figure 15. Mode shapes of the SMART 2013 RC structure for the model Case 1.

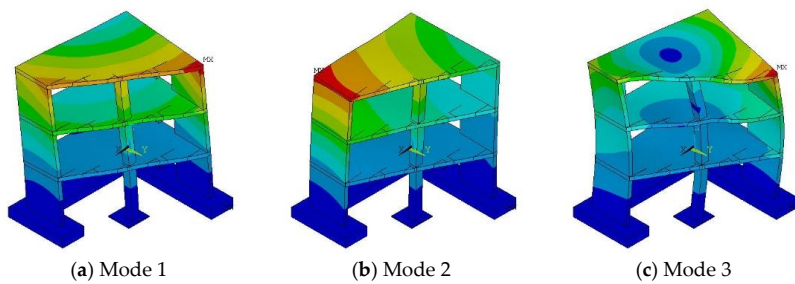


Figure 16. Mode shapes of the SMART 2013 RC structure for the model Case 2.

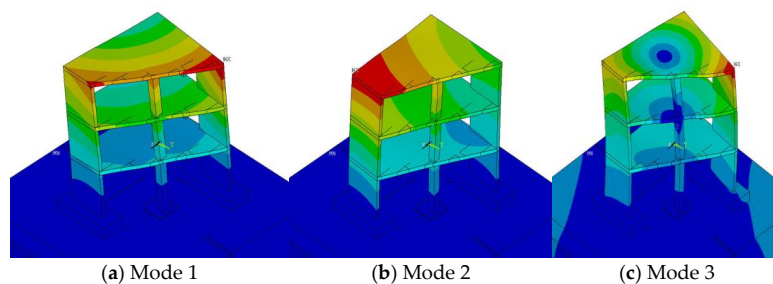


Figure 17. Mode shapes of the SMART 2013 RC structure for the model Case 3.

4.2. Seismic Analysis to Low-Intensity Ground Motions

Alongside the modal analysis result, the seismic response of the SMART 2013 structure to low-intensity ground motions was investigated. A classical Rayleigh damping was introduced to the SMART 2013 RC building with the following equation:

$$C = \alpha M + \beta K \tag{10}$$

where **M** and **K** are the mass and stiffness matrices of the structure, respectively. The two coefficients α and β are determined by solving the following system of equations:

$$\frac{1}{2} \begin{bmatrix} 1/\omega_i & \omega_i \\ 1/\omega_j & \omega_j \end{bmatrix} \begin{bmatrix} \alpha \\ \beta \end{bmatrix} = \begin{bmatrix} \zeta_i \\ \zeta_j \end{bmatrix} \tag{11}$$

where ω_i and ω_j are the natural frequencies corresponding to modes i and j , respectively, and ζ_i and ζ_j are the modal damping ratios for each mode. Table 6 shows the natural frequencies of the first three modes, and the corresponding modal damping ratios obtained by modal experiments. The modal damping ratios were obtained by analyzing the response of the structure with 28 accelerometers under the low-level (PGA < 0.1 g) biaxial random ground motion using a stochastic subspace identification bottom approach [23]. The coefficients α and β were calculated by solving Equation (11) using the frequencies and damping ratios for the first and second modes. The calculated α and β are -1.649 and 0.002 , respectively.

Table 6. Modal damping ratios obtained by experiments.

Mode	Frequency, f (Hz)	Modal Damping Ratio, ζ
1	6.28	0.026
2	7.86	0.042
3	16.50	0.055

Figure 18 shows the time history of the low-intensity ground motion. The time signal is the one scaled by 50% from the Northridge earthquake. The PGA is about 0.1 g in both the x and y directions. The structural response to the ground motion is calculated without considering material nonlinearity. Figures 19–21 show the seismic response of each floor of the SMART 2013 RC structure to the low-intensity ground motion at sampling point A. The calculated displacement and acceleration showed excellent agreement with the experimental results.

Table 7 presents the absolute maximum seismic response of the structure at the sampling point A. Both the displacement and acceleration values agreed quite well with the experimental results.

Table 7. Absolute maximum seismic responses at point A due to the low-intensity ground motions.

Floor	Displacement, u_x (mm)		Acceleration, a_x (m/s ²)	
	Analysis	Experiment	Analysis	Experiment
1st floor	1.06	0.91	1.37 (0.14 g)	1.29 (0.13 g)
2nd floor	1.08	1.00	1.88 (0.19 g)	1.74 (0.18 g)
3rd floor	1.10	1.01	2.66 (0.27 g)	2.49 (0.25 g)

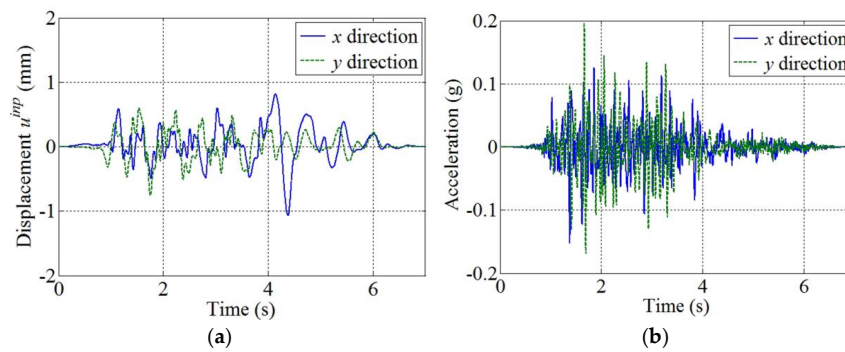


Figure 18. Low-intensity ground motions; (a) ground displacement; (b) ground acceleration.

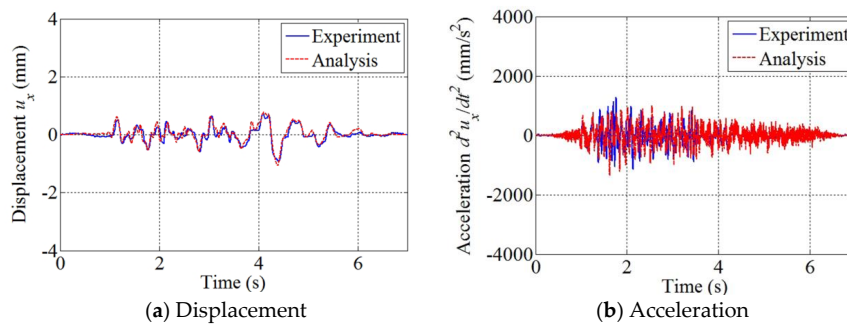


Figure 19. First-floor response in the x direction due to the low-intensity ground motion; responses sampled at point A.

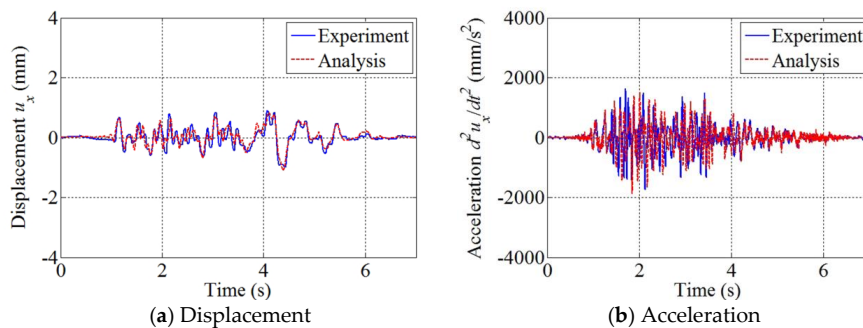


Figure 20. Second-floor response in the x direction due to the low-intensity ground motion; responses sampled at point A.

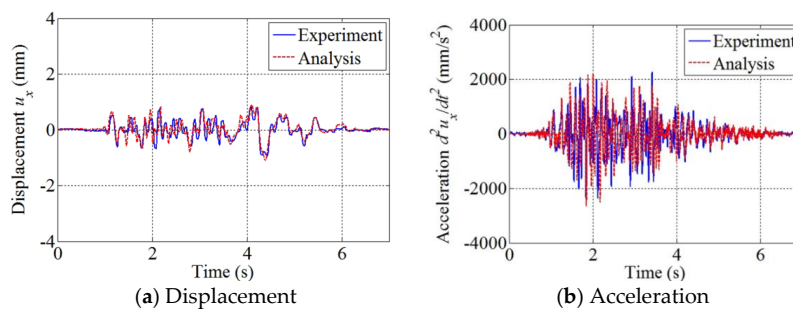


Figure 21. Third-floor response in the x direction due to the low-intensity ground motion; responses sampled at point A.

5. Nonlinear Seismic Response of the SMART 2013 RC Structure

After the seismic simulation to the low-intensity ground motion, the inelastic seismic response of the asymmetric three-storey RC structure subjected to high-intensity ground motions was investigated. Such a nonlinear analysis was part of the SMART 2013 international benchmark. The analysis case consisted of several simulations for three different seismic sequences: the design signal (Run 9), the Northridge earthquake main shocks (Run 11, Run 13, Run 17, and Run 19), and the Northridge aftershock (Run 21 and Run 23). The “Runs” are different regarding the strength of the ground motions. The PGA of each ground motion is presented in Table 8. The ground motion of Run 19 is the unscaled Northridge earthquake with PGAs of 1.1 g and 1.0 g in the x and y directions, respectively. Figure 22 shows the time history of the input ground motion used for the nonlinear seismic analysis.

Table 8. Nominal input ground motions for a nonlinear seismic analysis.

Run	PGA X (g)	PGA Y (g)	Percentage of Nominal Signal (%)	Type
9	0.22	0.23	100	Design earthquake signal–nominal
11	0.21	0.16	11	Scaled Northridge earthquake–step 1
13	0.40	0.21	22	Scaled Northridge earthquake–step 2
17	0.60	0.40	44	Scaled Northridge earthquake–step 3
19	1.10	1.00	100	Real Northridge earthquake–nominal
21	0.14	0.14	33	Scaled Northridge aftershock–step 1
23	0.70	0.40	100	Real Northridge aftershock–nominal

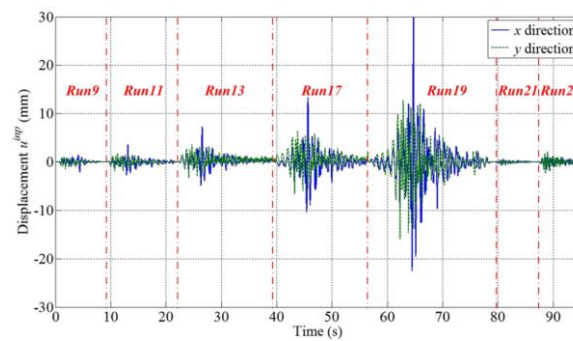


Figure 22. High-intensity ground motions for a nonlinear seismic analysis of the SMART 2013 structure.

First, the ground displacement of Run 9 was applied to the structure at the actuator locations of the shaking table. Figure 23 shows the experimental and numerical responses of the structure in the x direction sampled at point A of the third floor. The numerical response agreed well with the experimental result. The absolute maximum values of displacement and acceleration obtained from the shaking table test were 2.02 mm and 4100 mm/s², respectively. They are about twice as high as the responses to the low-intensity ground motion in Section 4.2, where the earthquake signal is scaled by 50%.

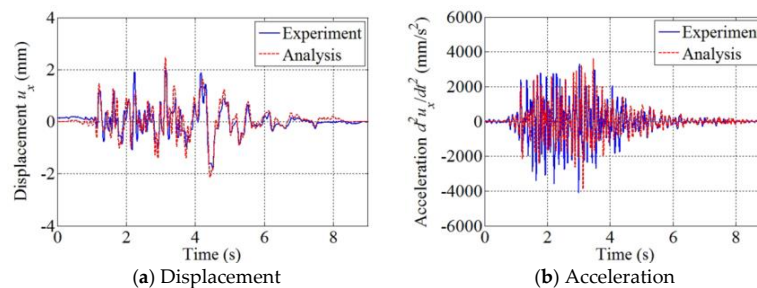


Figure 23. Numerical and experimental responses in the x direction due to the ground motion of Run 9; responses sampled at point A on the third floor.

Following Run 9, the Northridge earthquake’s main shocks (Run 11, Run 13, Run 17, and Run 19) with successively increasing PGA were applied to the structure at the actuator locations of the shaking table. Figures 24–27 show the displacement and acceleration at point A of the third floor. Overall, the numerical responses agreed well with experimental results, even during the high-intensity ground motions. The response was largest in the case of Run 19, where the absolute maximum displacement and acceleration were 36.73 mm and 22,420 mm/s² (2.28 g), respectively. These values are about 13.4 and 5.8 times higher than the calculated responses from Run 9, respectively.

In Run 13, the numerical response does not reflect the high-frequency experimental response well after about 5 s. This difference in response may be due to a gradual error in predicting structural stiffness during numerical analysis [34,35]. Despite the partial difference between the numerical and experimental results, the computed displacement and acceleration appear to capture the general trend of the experimental seismic behavior of the structure. After Run 13, the first three natural frequencies of the structure decreased by 26.66%, 19.98%, and 17.72%, respectively. These results implied that the stiffness of the SMART 2013 RC structure decreased after Run 13 compared to its initial stiffness. In the shaking table test corresponding to Run 13, significant cracks began to develop at the lower part of concrete walls and the column.

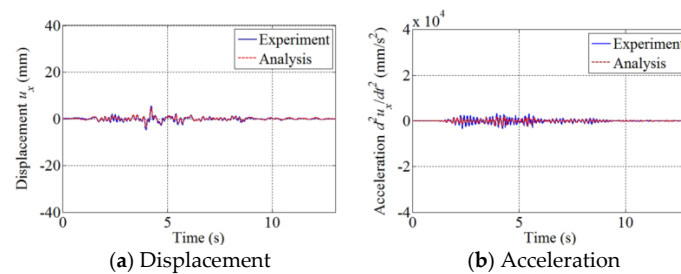


Figure 24. Numerical and experimental responses in the x direction due to the scaled Northridge earthquake of Run 11; responses sampled at point A on the third floor.

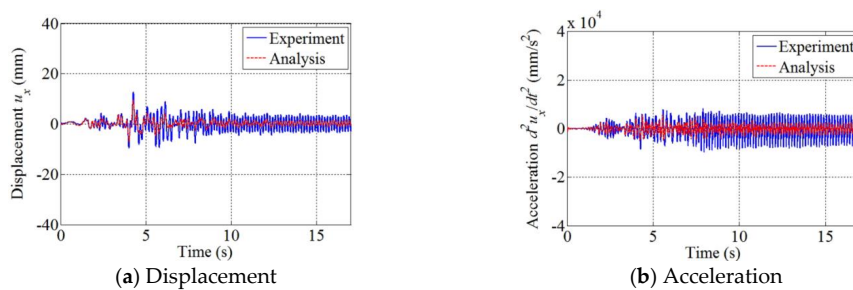


Figure 25. Numerical and experimental responses in the x direction due to the scaled Northridge earthquake of Run 13; responses sampled at point A on the third floor.

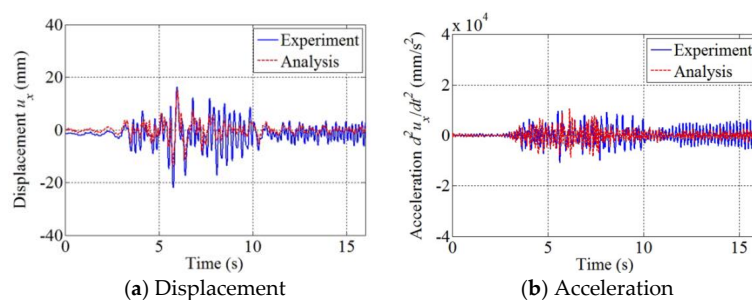


Figure 26. Numerical and experimental responses in the x direction due to the scaled Northridge earthquake of Run 17; responses sampled at point A on the third floor.

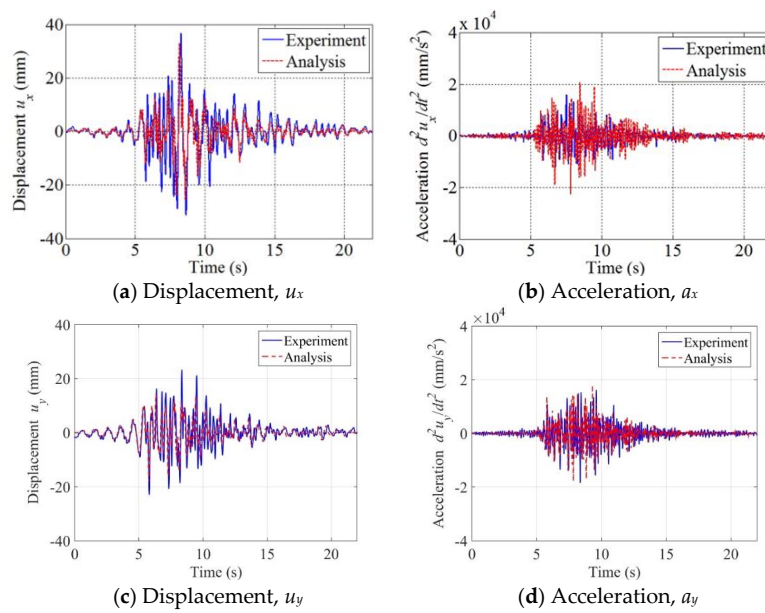


Figure 27. Numerical and experimental responses due to real Northridge earthquake of Run 19; responses sampled at point A on the third floor.

Figures 28 and 29 show the numerical and experimental responses of the SMART 2013 RC structure for the Northridge aftershock (Run 21 and Run 23). Overall, the numerical results reflected the experimental results, although there was a slight phase difference in the result of Run 23. The difference could be because the numerical model did not accurately reflect the stiffness degradation after severe damage to the structure. The cumulative error of numerical solutions of earlier seismic sequences might have also influenced the response difference. Tables 9 and 10 present the absolute maximum displacement and acceleration, respectively, that were calculated from each simulation stage. The displacement error was less than 10% for Run 19, wherein the ground motion was the strongest, whereas the error was around 20–30% for other runs. Table 11 shows the absolute maximum seismic responses at sampling points A to D in both the x and y directions for the case of Run 19. Although the peak values were somewhat different from the experimental values, the time histories in Figures 23–29 show that the numerical solution had a similar tendency to the response obtained from the experiment. Figure 30 shows the concrete walls after the shaking table test corresponding to Runs 13–19. Severe cracks and spalling of concrete occurred at the lower part of the concrete walls and the column connected to the foundation. Figures 31 and 32 show the Fourier frequency spectrum of displacement in the x and y directions, respectively, for Runs 17, 19, and 21. Overall, the spectra show a good agreement with those obtained from the experiment, particularly in the frequency range up to about 3 Hz.

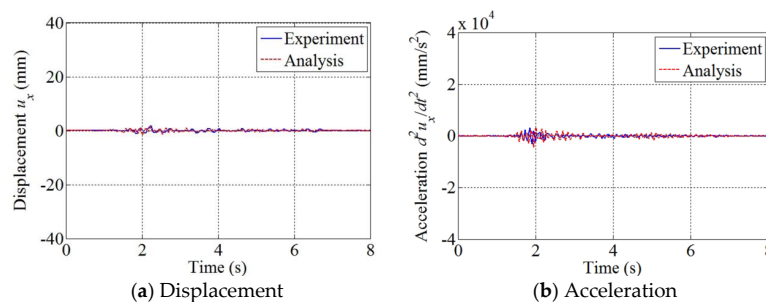


Figure 28. Numerical and experimental responses in the x direction due to the scaled Northridge aftershock of Run 21; responses sampled at point A on the third floor.

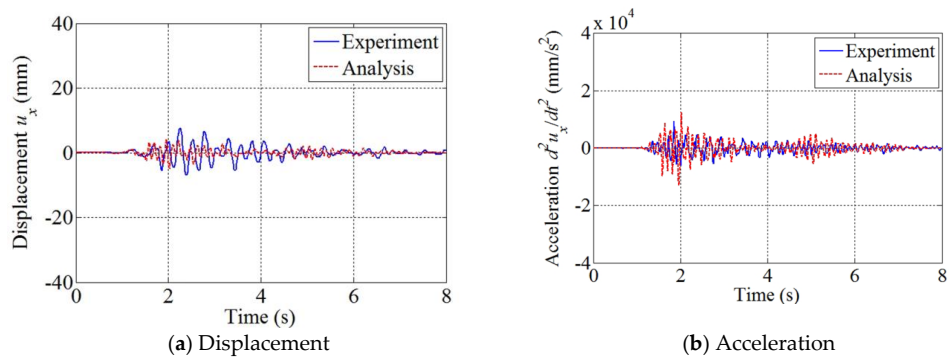


Figure 29. Numerical and experimental responses in the x direction due to real Northridge aftershock of Run 23; responses sampled at point A on the third floor.

Table 9. Absolute maximum displacement at point A on the third floor.

Seismic Simulation	Absolute Maximum Displacement, u_x		
	Analysis (mm)	Experiment (mm)	Error (%)
Run 9	2.47	2.02	22.28
Run 11	4.83	5.57	13.29
Run 13	9.51	12.92	26.39
Run 17	15.23	22.02	30.84
Run 19	33.09	36.73	9.91
Run 21	1.53	1.79	14.53
Run 23	4.93	7.66	35.64

Table 10. Absolute maximum acceleration at point A on the third floor.

Seismic Simulation	Absolute Maximum Acceleration, a_x		
	Analysis (m/s^2)	Experiment (m/s^2)	Error (%)
Run 9	3.88 (0.40 g)	4.10 (0.42 g)	5.37
Run 11	2.46 (0.25 g)	3.39 (0.34 g)	27.43
Run 13	5.67 (0.58 g)	9.73 (0.99 g)	41.73
Run 17	10.50 (1.07 g)	10.83 (1.10 g)	3.05
Run 19	22.42 (2.28 g)	16.11 (1.64 g)	39.17
Run 21	4.42 (0.45 g)	3.23 (0.33 g)	36.84
Run 23	13.15 (1.34 g)	9.28 (0.95 g)	41.70

Table 11. Absolute maximum seismic responses at sampling points A to D in both x and y directions for the analysis case of Run 19.

	A			B			C			D		
	Anal.	Exper.	Error (%)									
u_x (mm)	33.09	36.79	10.06	33.03	35.34	6.54	33.90	51.67	34.39	35.81	85.39	58.06
u_y (mm)	17.96	23.20	22.59	22.74	55.89	59.31	22.77	55.36	58.87	17.95	22.31	19.54
a_x (m/s^2)	22.42	16.11	39.17	20.27	14.61	38.74	25.52	16.78	52.09	34.32	32.01	7.22
a_y (m/s^2)	18.05	18.37	1.74	31.76	26.89	18.11	31.95	27.80	14.93	17.67	17.57	0.57

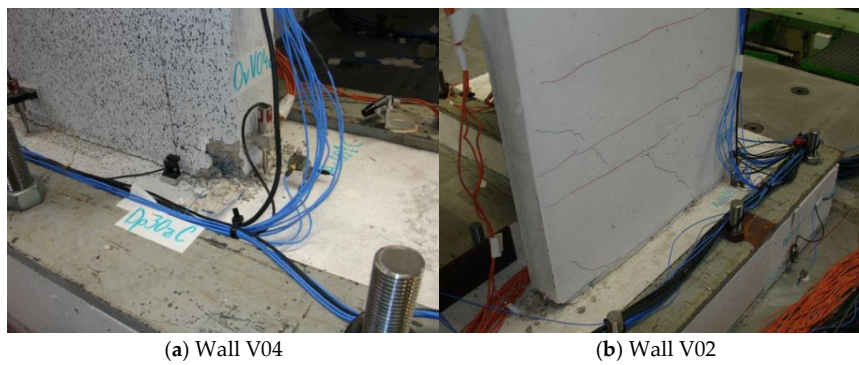


Figure 30. Damages in the lower part of the concrete walls connected to the foundation [23,30].

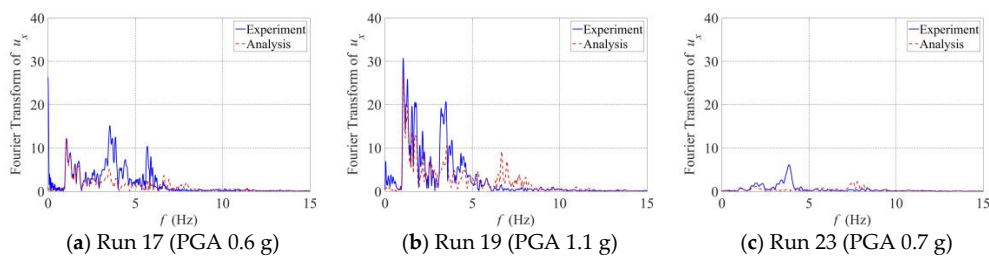


Figure 31. Frequency spectrum of the x directional displacement at point A on the third floor.

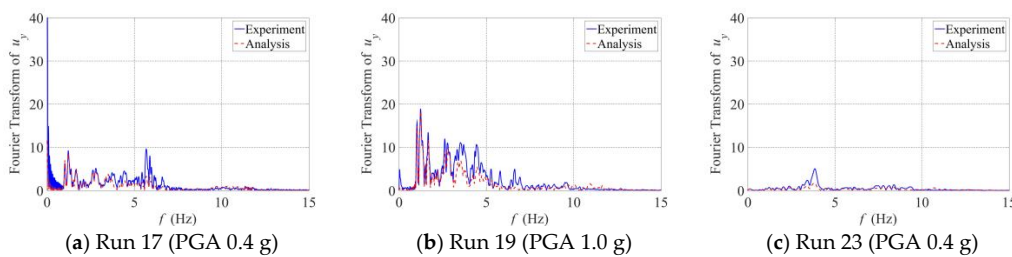


Figure 32. Frequency spectrum of the y directional displacement at point A on the third floor.

6. Torsional Behavior

The SMART 2013 RC structure is asymmetric in plan view, as shown in Figure 2. In general, asymmetric structures often exhibit coupled flexural and torsional behaviors against lateral loads, since the line of action of the lateral load does not pass through the center of the stiffness of the structure when viewed in plan [36–41]. Figure 33 shows the displacement trace at the sampling points of the third floor of the building during the Northridge main shock with Run 19. The displacement traces indicate that the building was not only bent by seismic forces, but also twisted. Figure 34 shows the distortion of each floor of the building at 8.6 s, when the seismic response was the largest, as can be seen in Figure 27. For the calculated torsional response, the phase was similar to what was obtained from the shaking table test. Furthermore, the calculated torsional response seems to reflect the test result in that the degree of twist was more substantial on the higher floors. However, the numerical plan view deformation seems to be more correlated to a horizontal translation rather than a twisting mode. The difference could be because the numerical model did not accurately reflect the reduced torsional stiffness of the damaged structure.

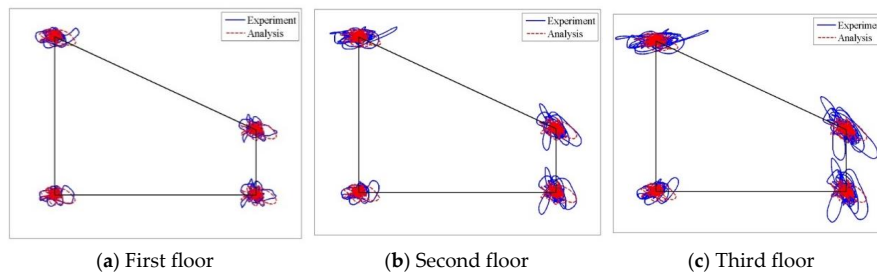


Figure 33. Displacement trace at sampling points during the Northridge main shock of Run 19.

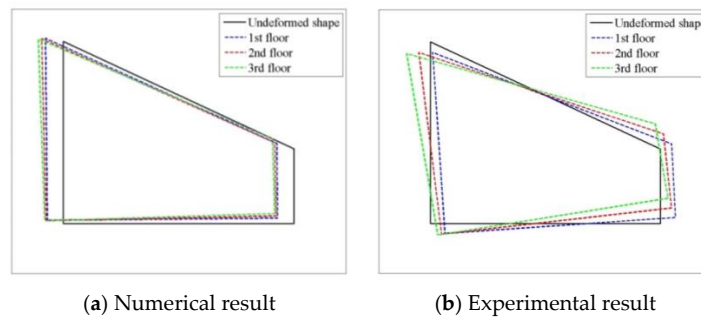


Figure 34. Distortion of each floor due to the Northridge main shock (Run 19) at 8.6 s.

In order to further investigate the torsional effect, we compared the seismic response of the asymmetric SMART 2013 structure with the response of a hypothetical symmetric structure. Figure 35 shows a plan view of the symmetric structure and the corresponding three-dimensional finite element model. The number of floors, thickness of the floors and walls, dimensions of the column, length in the x and y directions, mass of each floor, and materials used were the same as for the asymmetric SMART 2013 structure.

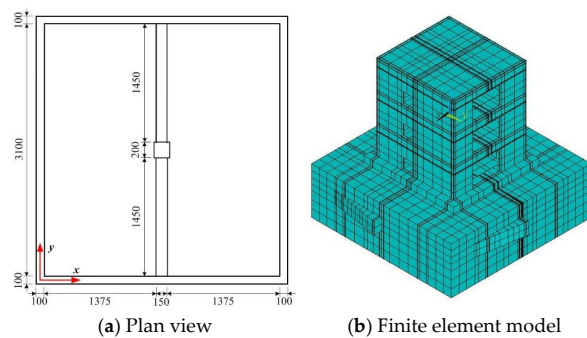


Figure 35. Finite element modeling of a hypothetical symmetric structure for comparison with the SMART 2013 RC structure.

In Figure 36, the displacement responses of the asymmetric SMART 2013 structure and the hypothetical symmetric structure due to the Northridge main shock are compared with each other. The responses are sampled at point D. On the first floor, the responses were similar to each other. However, the difference in response became more substantial on the higher floors. The tendency of the greater response of the asymmetric structure also appeared in the frequency response spectrum, as shown in Figure 37. Figures 38 and 39 compare the absolute maximum displacement for the two cases. For all of the sampling points and all of the floors, the displacement response of the asymmetric structure was larger than that of the hypothetical symmetric structure. It can also be seen that the response difference increased on the higher floors. The difference in the x directional absolute

maximum displacement between the asymmetric and symmetric structures was up to 15%, while the difference in the y directional absolute maximum displacement was up to 31%. The results indicate that, similar to previous studies [36–41], a larger seismic response should be considered in the seismic design of an asymmetric structure compared to a symmetric structure with same design conditions.

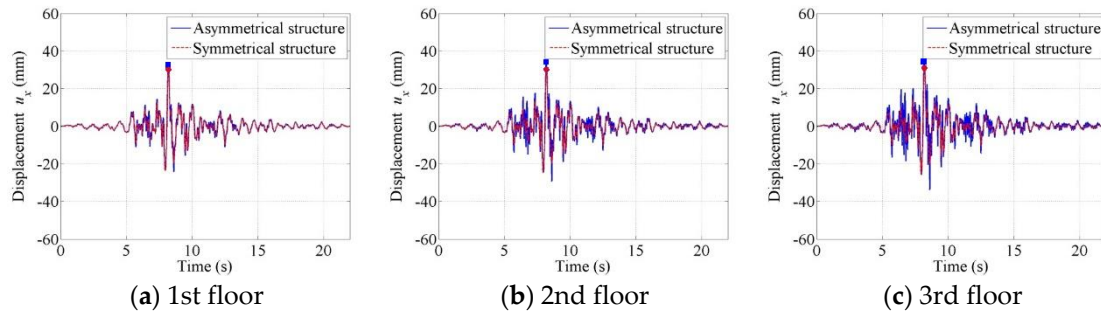


Figure 36. Displacement responses of the asymmetric SMART 2013 structure and the hypothetical symmetric structure due to the Northridge earthquake (Run 19); Responses sampled at point D.

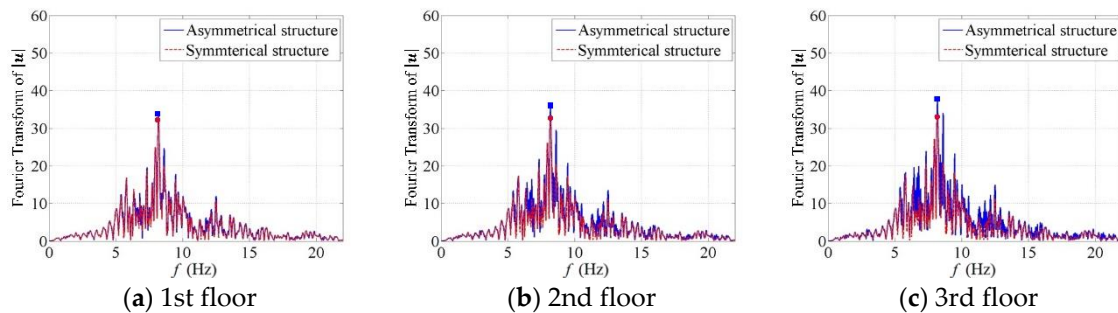


Figure 37. Displacement frequency spectra of the asymmetric SMART 2013 structure and the hypothetical symmetric structure due to the Northridge earthquake (Run 19); Displacement amplitude $(|u| = \sqrt{u_x^2 + u_y^2})$ sampled at point D.

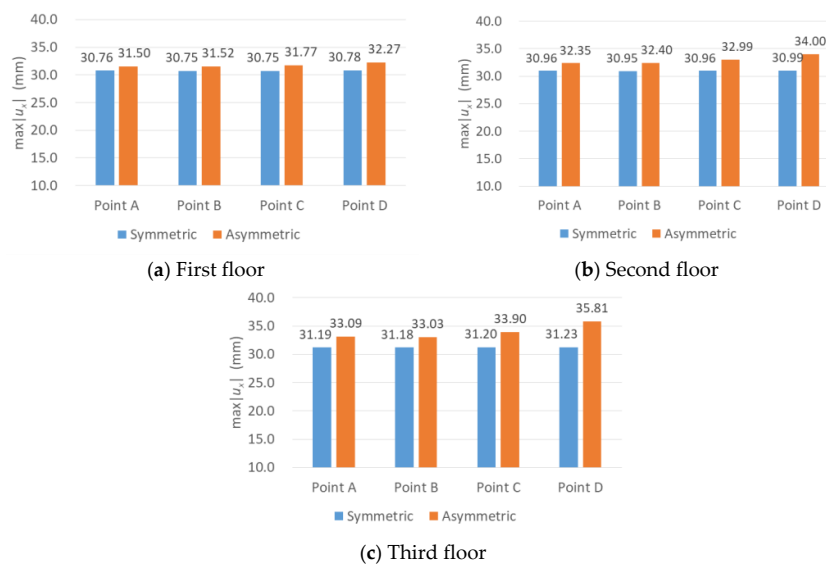


Figure 38. Absolute maximum displacement in the x-direction of the asymmetric and the hypothetical symmetric structures due to the Northridge earthquake (Run 19).

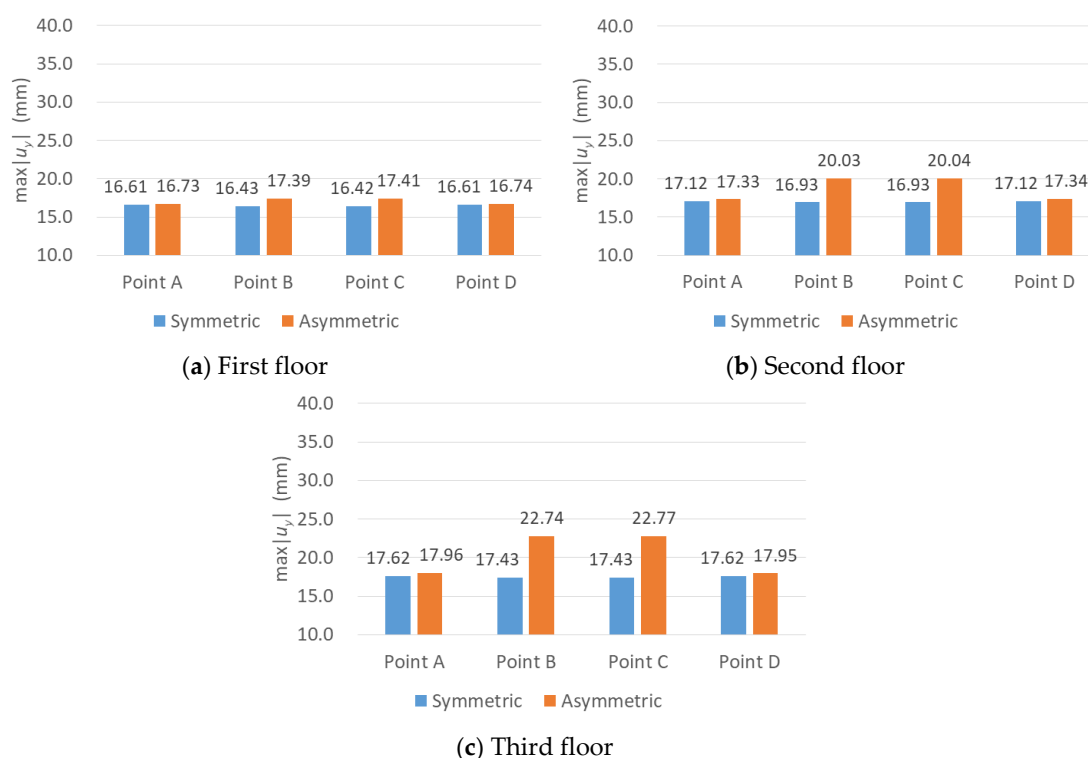


Figure 39. Absolute maximum displacement in the y direction of the asymmetric and the hypothetical symmetric structures due to the Northridge earthquake (Run 19).

7. Conclusions

This study presented the finite element modeling and simulation of the asymmetric SMART 2013 RC structure, considering torsional effect and material nonlinearity. Local tests with a representative volume element validated the nonlinear constitutive models set up for concrete and steel reinforcement. The computed first three natural frequencies were 6.26 Hz, 7.77 Hz, and 13.15 Hz, respectively, which were close to the experimental results. In the seismic analysis with low-intensity ground motions, the displacement and acceleration calculated at sampling points showed good agreement with the experimental results. In the blind seismic simulation, the consecutive seismic sequence of design signal, Northridge main shock, and Northridge aftershock were used to calculate the seismic response of the SMART 2013 RC structure at each floor. The time history of displacement and acceleration, as well as their frequency spectrum, agreed reasonably with the result of the shaking table test that was conducted as part of the international benchmark. By investigating the torsional behavior of the asymmetric SMART 2013 structure due to the seismic load, it was shown that the seismic response of the asymmetric structure was larger than that of the hypothetical symmetric structure. The response difference increased on the higher floors. The result indicates that a larger seismic response should be considered in the seismic design of an asymmetric structure compared to a symmetric structure with similar design conditions.

Acknowledgments: This research was supported by the Korea Institute of Nuclear Safety (Grant No. 14-51) and by the Korea Institute of Energy Technology Evaluation and Planning (KETEP) Grant (No. 20151510400100) funded by the Ministry of Trade, Industry and Energy of the Republic of Korea.

Author Contributions: Hyun-Kyu Lim, Jun Won Kang and Ho-Seok Chi conceived the main idea of this work; Hyun-Kyu Lim prepared this article as the first author; Hyun-Kyu Lim, Jun Won Kang, Hongrak Pak and Young-Geun Lee contributed finite element simulation; Hyun-Kyu Lim, Jun Won Kang and Janghwan Kim analyzed the numerical and experimental data; Hyun-Kyu Lim and Jun Won Kang wrote the paper.

Conflicts of Interest: The authors declare no conflict of interest.

References

- Bhattacharjee, S.S.; Léger, P. Concrete constitutive models for nonlinear seismic analysis of gravity dams—State-of-the-art. *Can. J. Civ. Eng.* **1992**, *19*, 492–509. [[CrossRef](#)]
- Willam, K.J. Encyclopedia of Physical Science and Technology. In *Constitutive Models for Engineering Materials*, 3rd ed.; Academic Press: San Diego, CA, USA, 2002; Volume 3, pp. 3603–3633.
- Chen, W.F. *Plasticity in Reinforced Concrete*; J. Ross Publishing: New York, NY, USA, 2007.
- Kim, T.H.; Kim, Y.J.; Shin, H.M. Seismic performance assessment of reinforced concrete bridge piers supported by laminated rubber bearings. *Struct. Eng. Mech.* **2008**, *29*, 259–278. [[CrossRef](#)]
- Jayalekshmi, B.R.; Deepthi, V.G.; Venkataramana, K.; Shivashankar, R. Seismic response analysis of reinforced concrete frames including soil flexibility. *Struct. Eng. Mech.* **2013**, *48*, 1–16. [[CrossRef](#)]
- Fardis, M.N.; Biskinis, D.E. Deformation capacity of RC members, as controlled by flexure or shear. In Proceedings of the Otani Symposium 2003, Tokyo, Japan, 8–9 September 2003; Volume 511530.
- Haselton, C.B.; Deierlein, G.G. *Assessing Seismic Collapse Safety of Modern Reinforced Concrete Frame Buildings*; PEER Report 2007/08; PEER Center, University of California: Berkeley, CA, USA, 2007.
- Ibarra, L.F.; Medina, R.A.; Krawinkler, H. Hysteretic models that incorporate strength and stiffness deterioration. *Earthq. Eng. Struct. Dyn.* **2005**, *34*, 1489–1511. [[CrossRef](#)]
- Fischinger, M.; Rejec, K.; Isakovic, T. Modeling Inelastic Shear Response of RC Walls. In Proceedings of the 15th World Conference on Earthquake Engineering, Lisbon, Portugal, 24–28 September 2012.
- Ueda, M.; Seya, H.; Ohmiya, Y.; Taniguchi, H.; Kambayashi, A. Nonlinear analysis on RC shear wall shaking table test. In Proceedings of the 14th International Conference on Structural Mechanics in Reactor Technology, Lyon, France, 17–22 August 1997.
- Ile, N.; Reynouard, J.M. Nonlinear analysis of reinforced concrete shear wall under earthquake loading. *J. Earthq. Eng.* **2000**, *4*, 183–214. [[CrossRef](#)]
- Richard, B.; Ile, N.; Frau, A.; Ma, A.; Loiseau, O.; Giry, C.; Ragueneau, F. Experimental and numerical study of a half-scaled reinforced concrete building equipped with thermal break components subjected to seismic loading up to severe damage state. *Eng. Struct.* **2015**, *92*, 29–45. [[CrossRef](#)]
- Pegon, P.; Magonette, G.; Molina, F.J.; Verzeletti, G.; Dyngeland, T.; Negro, P.; Tognoli, P. *Programme SAFE: Rapport du Test T5*; Unité Mécanique des Structures, Institut des Systèmes, de l'Informatique et de la Sécurité, Centre Commun de Recherche, Commission Européenne: Ispra, Italy, 1998; p. 21020.
- Bisch, P.; Coin, A. The CASSBA project. In Proceedings of the 10th European Conference on Earthquake Engineering, Vienna, Austria, 28 August–2 September 1994.
- Bisch, P.; Coin, A. The CAMUS research program. In Proceedings of the 11th European Conference on Earthquake Engineering, Paris, France, 6–11 September 1998.
- Richard, B.; Martinelli, P.; Voldoire, F.; Corus, M.; Chaudat, T.; Abouri, S.; Bonfils, N. SMART 2008: Shaking table tests on an asymmetrical reinforced concrete structure and seismic margins assessment. *Eng. Struct.* **2015**, *105*, 48–61. [[CrossRef](#)]
- Richard, B.; Martinelli, P.; Voldoire, F.; Chaudat, T.; Abouri, S.; Bonfils, N. SMART 2008: Overview, synthesis and lessons learned from the International Benchmark. *Eng. Struct.* **2016**, *106*, 166–178. [[CrossRef](#)]
- Panagiotou, M.; Restrepo, J.I.; Conte, J.P. Shake-table test of a full-scale 7-story building slice. Phase I: Rectangular wall. *J. Struct. Eng.* **2010**, *137*, 691–704. [[CrossRef](#)]
- Negro, P.; Verzeletti, G.; Magonette, G.E.; Pinto, A.V. *Tests on a Fourstorey Full-Scale R/C Frame Designed According to Eurocodes 8 and 2: Preliminary Report*; Report EUR, 15879; Joint Research Centre: Ispra, Italy, 1994.
- Magliulo, G.; Ramasco, R. Seismic response of three-dimensional r/c multi-storey frame building under uni- and bi-directional input ground motion. *Earthq. Eng. Struct. Dyn.* **2007**, *36*, 1641–1657. [[CrossRef](#)]
- Jeong, S.H.; Elnashai, A.S. Analytical assessment of an irregular RC frame for full-scale 3D pseudo-dynamic testing part I: Analytical model verification. *J. Earthq. Eng.* **2005**, *9*, 95–128. [[CrossRef](#)]
- Jeong, S.H.; Elnashai, A.S. Analytical assessment of an irregular RC frame for full-scale 3D pseudo-dynamic testing part II: Condition assessment and test deployment. *J. Earthq. Eng.* **2005**, *9*, 265–284. [[CrossRef](#)]
- Chaudat, T.; Charbonnel, P.E.; Garnier, C.; Le Corre, M.; Mahé, M.; Poupin, S.; Vasic, S. *SMART 2013 Test Report*; SEMT/EMSI/NT/14-019; French Alternative Energies and Atomic Commission: Gif-sur-Yvette, France, 2014.

24. Richard, B.; Fontan, M.; Mazars, J. *SMART-2013: Overview, Synthesis and Lessons Learnt from the International Benchmark*; SEMT/EMSI/NT/14-037; French Alternative Energies and Atomic Commission: Gif-sur-Yvette, France, 2014.
25. Richard, B.; Voldoire, F.; Fontan, M.; Mazars, J.; Chaudat, T.; Abouri, S.; Bonfils, N. SMART 2013: Lessons learned from the international benchmark about the seismic margin assessment of nuclear RC buildings. *Eng. Struct.* **2018**, *161*, 207–222. [[CrossRef](#)]
26. Richard, B.; Cherubini, S.; Voldoire, F.; Charbonnel, P.E.; Chaudat, T.; Abouri, S.; Bonfils, N. SMART 2013: Experimental and numerical assessment of the dynamic behavior by shaking table tests of an asymmetrical reinforced concrete structure subjected to high intensity ground motions. *Eng. Struct.* **2016**, *109*, 99–116. [[CrossRef](#)]
27. Kachlakev, D.; Miller, T. *Finite Element Modeling of Reinforced Concrete Structures Strengthened with FRP Laminates-Final Report: 2001*; FHWA-OR-RD-01-17; Oregon Department of Transportation: Salem, OR, USA, 2001.
28. ANSYS Inc. *ANSYS Mechanical APDL, Release 14.5*; ANSYS Inc.: Canonsburg, PA, USA, 2012.
29. Willam, K.J.; Warnke, E.P. Constitutive models for the triaxial behavior of concrete. *Int. Assoc. Bridge Struct. Eng.* **1975**, *19*, 1–30.
30. Richard, B.; Charbonnel, P.E. *SMART 2013 International Benchmark Experimental Data for Stage #2*; SEMT/EMSI/NT/13-035/A; French Alternative Energies and Atomic Commission: Gif-sur-Yvette, France, 2013.
31. Chaudat, M.; Benjamin, R. *SMART 2013 Data Acquisition Project*; SEMT/EMSI/NT/13-003; French Alternative Energies and Atomic Commission: Gif-sur-Yvette, France, 2013.
32. Crijanovschi, S.; Richard, B.; Chaudat, T.; Atanasiu, G.M. Preliminary numerical analysis of a reinforced concrete mock up: Effects of thermal breakers and shaking table. In Proceedings of the 15th World Conference on Earthquake Engineering, Lisbon, Portugal, 24–28 September 2012.
33. Juster-Lermitte, S.; Chaudat, T.; Zenter, I.; Courtois, A. *Project SMART 2008*; SEMT/EMSI/RT/09-011A; French Alternative Energies and Atomic Commission: Gif-sur-Yvette, France, 2009.
34. Richard, B.; Ragueneau, F. Nonlinear analysis of a reinforced concrete mock-up under seismic loading. In Proceedings of the 15th World Conference on Earthquake Engineering, Lisbon, Portugal, 24–28 September 2012.
35. Richard, B.; Ragueneau, F. Continuum damage mechanics based model for quasi brittle materials subjected to cyclic loadings: Formulation, numerical implementation and applications. *Eng. Fract. Mech.* **2013**, *98*, 383–406. [[CrossRef](#)]
36. Paulay, T. Some design principles relevant to torsional phenomena in ductile buildings. *J. Earthq. Eng.* **2001**, *5*, 273–308. [[CrossRef](#)]
37. Rutenberg, A. EAEE Task Group (TG) 8: Behaviour of irregular and complex structures, asymmetric structures—Progress since 1998. In Proceedings of the 12th European Conference on Earthquake Engineering, London, UK, 9–13 September 2002. Paper No. 832.
38. Stathopoulos, K.G.; Anagnostopoulos, S.A. Inelastic earthquake induced torsion in buildings: Results and conclusions from realistic models. In Proceedings of the 12th European Conference on Earthquake Engineering, London, UK, 9–13 September 2002.
39. Garcia, O.; Islas, A.; Ayala, A.G. Effect of the in-plan distribution of strength on the non-linear seismic response of torsionally coupled buildings. In Proceedings of the 13th World Conference on Earthquake Engineering, Vancouver, BC, Canada, 1–6 August 2004.
40. Magliulo, G.; Maddaloni, G.; Petrone, C. Influence of earthquake direction on the seismic response of irregular plan RC frame buildings. *Earthq. Eng. Eng. Vib.* **2014**, *13*, 243–256. [[CrossRef](#)]
41. Llera, J.C.D.L.; Chopra, A.K. Inelastic behavior of asymmetric multistory buildings. *J. Struct. Eng.* **1996**, *122*, 597–606. [[CrossRef](#)]

